

Supplementary Information for “Field-induced spin liquid in the decorated square-kagome antiferromagnet nabokoite $\text{KCu}_7\text{TeO}_4(\text{SO}_4)_5\text{Cl}$ ”

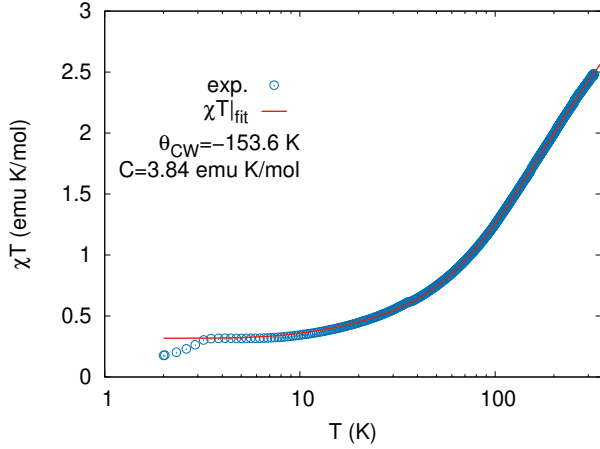
Matías G. Gonzalez,^{1,2} Yasir Iqbal,³ Johannes Reuther,^{1,2,3} and Harald O. Jeschke^{4,3}

¹Helmholtz-Zentrum Berlin für Materialien und Energie, Hahn-Meitner-Platz 1, 14109 Berlin, Germany

²Dahlem Center for Complex Quantum Systems and Fachbereich Physik, Freie Universität Berlin, 14195 Berlin, Germany

³Department of Physics and Quantum Centre of Excellence for Diamond and Emergent Materials (QuCenDiEM), Indian Institute of Technology Madras, Chennai 600036, India

⁴Research Institute for Interdisciplinary Science, Okayama University, Okayama 700-8530, Japan



Supplementary Figure 1. Magnetic susceptibility $\chi(T)$ of nabokoite from Ref. [S1], multiplied by temperature (symbols) and fit by the *ansatz* of Eq. (S1).

Supplementary Note 1. RE-EVALUATING THE EXPERIMENTAL SUSCEPTIBILITY

Nabokoite $\text{KCu}_7\text{TeO}_4(\text{SO}_4)_5\text{Cl}$ is a highly frustrated antiferromagnet, with ordering temperature $T_N = 3.2\text{K}$ strongly suppressed below the energy scale of magnetic interactions. We thus use a fitting *ansatz* developed recently by Pohle and Jaubert [S2] for spin liquids:

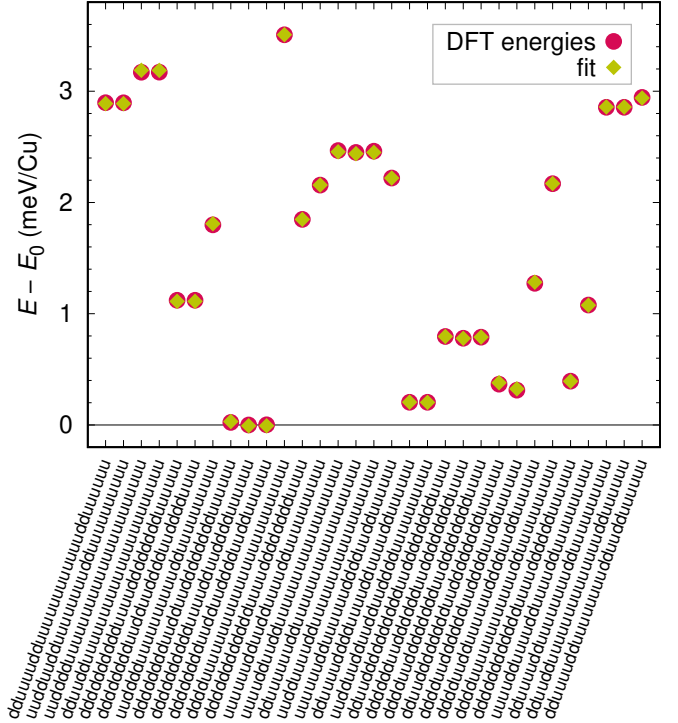
$$\chi T^{\text{fit}} = \frac{1 + b_1 \exp[c_1/T]}{a + b_2 \exp[c_2/T]} \quad (\text{S1})$$

$$C = \frac{1 + b_1}{a + b_2}, \quad \theta_{\text{CW}} = \frac{b_1 c_1}{1 + b_1} - \frac{b_2 c_2}{a + b_2}$$

The fit is shown in Supplementary Figure 1. It is excellent right down to the ordering temperature T_N and allows us to determine the Curie-Weiss temperature of nabokoite to $\theta_{\text{CW}} = -153.6\text{K}$. Note that a linear fit of χ^{-1} is not feasible for this materials [S1].

Supplementary Note 2. ADDITIONAL DFT DETAILS

In Supplementary Figure 2, we show a comparison between the DFT energies and the fit to the Heisenberg



Supplementary Figure 2. DFT total energies per Cu for 31 distinct spin configurations (circles). The fit to the Heisenberg Hamiltonian with 13 exchange interactions is excellent.

Hamiltonian with 13 exchange interactions. The agreement is very good. Small deviations are reflected in the statistical errors given in Supplementary Table 1 which contains the full energy mapping results. Exchange paths are identified by the Cu-Cu distances given in the last line. The first six exchange interactions are shown graphically in Fig. 1 a of the main text. The bold line in the table is the interpolated set of couplings which matches the Curie-Weiss temperature of $\theta_{\text{CW}} = -153.6\text{K}$. We calculate θ_{CW} according to

$$\theta_{\text{CW}} = -\frac{2}{3}S(S+1)\frac{2}{7}(2J_1 + 2J_2 + 2J_3 + J_4 + 2J_5 + 2J_6 + 2J_8 + 2J_9 + 2J_{10} + 2J_{11} + 2J_{12} + J_{16} + J_{18} + 2J_{20}) \quad (\text{S2})$$

Supplementary Table 1. Exchange interactions of nabokoite $\text{KCu}_7\text{TeO}_4(\text{SO}_4)_5\text{Cl}$ obtained by DFT energy mapping as described in the Methods section. The line in bold face corresponds to the set of couplings that match the experimental Curie-Weiss temperature. The distances d given in the last line are the Cu-Cu distances that identify the exchange paths.

U (eV)	J_1 (K)	J_2 (K)	J_3 (K)	J_4 (K)	J_5 (K)	J_6 (K)	J_8 (K)
5	25.3(6.7)	212.3(4.3)	248.3(4.8)	255.5(4.9)	241.0(2.3)	43.2(2.7)	-14.4(1.7)
5.5	19.4(5.3)	189.3(3.5)	229.7(3.9)	236.3(4.0)	222.8(1.9)	40.5(2.2)	-13.2(1.3)
6	14.3(4.3)	168.8(2.8)	212.2(3.1)	218.4(3.2)	204.3(1.5)	37.9(1.7)	-12.2(1.1)
7	5.4(2.8)	134.1(1.8)	179.9(2.1)	186.1(2.0)	170.1(1.0)	33.1(1.2)	-10.6(0.7)
7.5	2.7(2.2)	119.8(1.5)	166.5(1.6)	171.8(1.7)	154.0(0.8)	30.7(0.9)	-9.6(0.6)
7.55	2.4(1.8)	118.5(1.5)	165.2(1.6)	170.5(1.7)	152(0.8)	30.5(0.9)	-9.5(0.6)
8	-0.5(1.8)	106.7(1.2)	152.8(1.3)	158.4(1.3)	140.0(0.7)	28.6(0.8)	-9.0(0.5)
d (Å)	3.102	3.294	3.453	4.659	4.672	4.917	5.366
U (eV)	J_9 (K)	J_{11} (K)	J_{12} (K)	J_{16} (K)	J_{18} (K)	J_{20} (K)	θ_{CW} (K)
5	2.3(4.2)	-17.6(4.7)	-5.9(5.3)	-2.4(4.1)	0.1(2.4)	11.2(3.4)	-249
5.5	1.9(3.5)	-15.2(3.7)	-4.7(4.3)	-2.4(3.3)	0.1(1.9)	8.9(2.8)	-228
6	1.6(2.7)	-13.2(3.0)	-3.8(3.4)	-2.2(2.6)	0.1(1.5)	7.2(2.2)	-207
7	0.8(1.8)	-9.8(2.0)	-3.2(2.2)	-1.9(1.7)	0.1(1.1)	4.9(1.4)	-171
7.5	0.9(1.4)	-9.0(1.6)	-2.3(1.8)	-1.8(1.4)	0.1(0.8)	3.9(1.2)	-155
7.55	0.9(1.4)	-8.9(1.6)	-2.2(1.8)	-1.8(1.4)	0.1(0.8)	3.9(1.2)	-153.6
8	0.6(1.2)	-7.8(1.3)	-2.3(1.5)	-1.6(1.1)	0.0(0.7)	3.4(0.9)	-140
d (Å)	5.678	5.693	5.892	6.204	6.851	6.953	

Supplementary Note 3. CLASSICAL MONTE CARLO RESULTS ON THE 2D MODELS

The classical Monte Carlo (cMC) calculations are carried out as explained in the Methods section of the main article. For the 2D model, we use system sizes of $N = 7L^2$, where 7 is the number of sites in the unit cell and L is the number of unit cells in the two Cartesian directions. In each independent run, the energy and specific heat are calculated at every temperature by averaging through the second half of the Monte Carlo steps performed at each temperature. While the energy is calculated by a simple average, $e = \langle e \rangle$, the specific heat is calculated as

$$c_v(T) = N \frac{\langle e^2 \rangle - \langle e \rangle^2}{T^2} \quad (\text{S3})$$

The results are then averaged over 10 independent runs. The $c_v(T)$ calculations (after averaging) are shown in Supplementary Figure 3a, by the continuous lines for different system sizes from $L = 10$ ($N = 700$ spins) to $L = 80$ ($N = 44800$ spins).

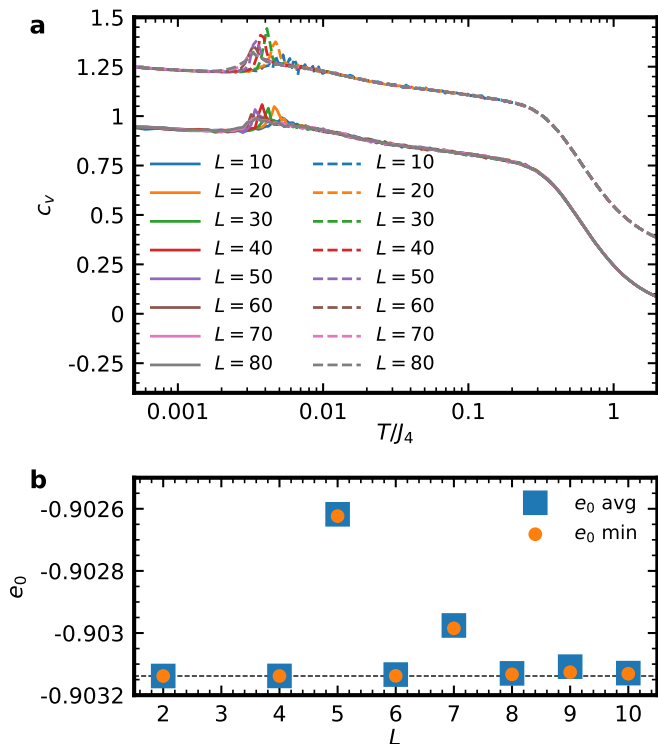
Another alternative is to calculate $c_v(T)$ as the derivative of $e(T)$ after averaging over independent runs. The results of this method are shown by the dashed lines in Supplementary Figure 3a, where an arbitrary 0.3 shift has been chosen to distinguish from the previous results. Although the two methods for obtaining $c_v(T)$ should be equivalent, one often encounters discrepancies. When this happens, it is usually an indication that the system is exhibiting problems in thermalizing. In this case, both curves agree well down to the lowest temperatures, and only differ slightly around the peak at $T = 0.004 J_4$. This peak is very faint and does not scale with system size, indicating that it is not a phase transition. Furthermore,

it seems to vanish with increasing system size. And since the continuous $\text{SU}(2)$ symmetry cannot be broken at finite temperatures in 2D systems, a phase transition (if there is such a transition) has to come from the breaking of an emergent discrete symmetry, none of which is broken in the ground state.

The ground-state energy of the system can be obtained as the continuation of a slow cooldown protocol to $T = 0$. In Supplementary Figure 3b we show these results for smaller lattices ranging from $L = 2$ to 10. The average ground-state energy is shown by the blue squares, while the orange dots show the minimum among the 10 independent runs for each lattice size. It becomes evident that all lattices with even L reach the same ground-state energy, even for lattices as small as $L = 2$ ($N = 28$ spins). On the other hand, the odd L lattices exhibit higher energies ($L = 3$ is out of scale), indicating that the periodic boundary conditions are introducing frustration into the system, while the even L lattices are unfrustrated.

As explained in the main text, this behaviour can be tracked to the spin pattern of the ground state, which requires 2 unit cells in each direction to repeat itself along independent zigzag lines of J_3 and J_5 . We show in Supplementary Figure 4 two examples of ground-state configurations for the $L = 2$ lattice. The arrows indicate the (S_x, S_y) components of the spins, while the colour determines S_z . For clarity, we rotate all the spins such that the bottom left apex spin is $\mathbf{S} = (0, 0, 1)$; therefore the green arrow with zero length. The direction of this arrow, as well as the other apex arrows, should be disregarded since it is just selected by a small numerical error in the (S_x, S_y) components. The important thing is that they are all dark green and have almost zero length.

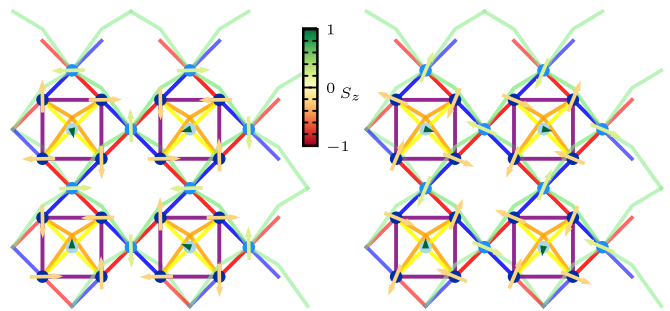
These states have already been described in the main text, but it is nonetheless important to revisit its fea-



Supplementary Figure 3. Classical Monte Carlo calculations for the 2D model for several sizes L . **a** Specific heat is calculated in two different ways (see text), where the dashed data is shifted by 0.3 to appreciate the difference. **b** Ground-state energy average over 10 independent runs (blue squares) and the lowest value among the runs (orange circle).

tures. All the base spins are slightly canted out of the (S_x, S_y) -plane and have a small negative S_z component, as can be seen by their yellowish-red colour. The link spins are also canted, but with positive values of S_z . Overall, base and link spins have only four different directions in the (S_x, S_y) -plane. The base spins connected by diagonal couplings J_4 (orange) are antiferromagnetically ordered in (S_x, S_y) , while they form $\pi/2$ angles with neighbouring spins connected by J_2 (purple). The base spins are then defined by pointing opposite [in (S_x, S_y, S_z)] to their neighbours connected by J_3 (red coupling).

Altogether, this is the four-coloured solution presented in the main text. The spins on zigzag lines (see main text) composed of base and link spins connected by J_4 and J_3 (orange and red bonds) can be transformed according to $(S_x, S_y, S_z) \rightarrow (-S_x, -S_y, S_z)$ while maintaining the same energy, staying in the ground-state manifold. This gives rise to the subextensive degeneracy since there are $2L$ lines in which these moves can be applied independently. When applying cMC to larger lattices, as the temperature is lowered, the system gets trapped into a particular state of the manifold which, however, is spatially diverse in the sense that it does not contain a repeated $L = 2$ cell. Therefore, large enough lattices



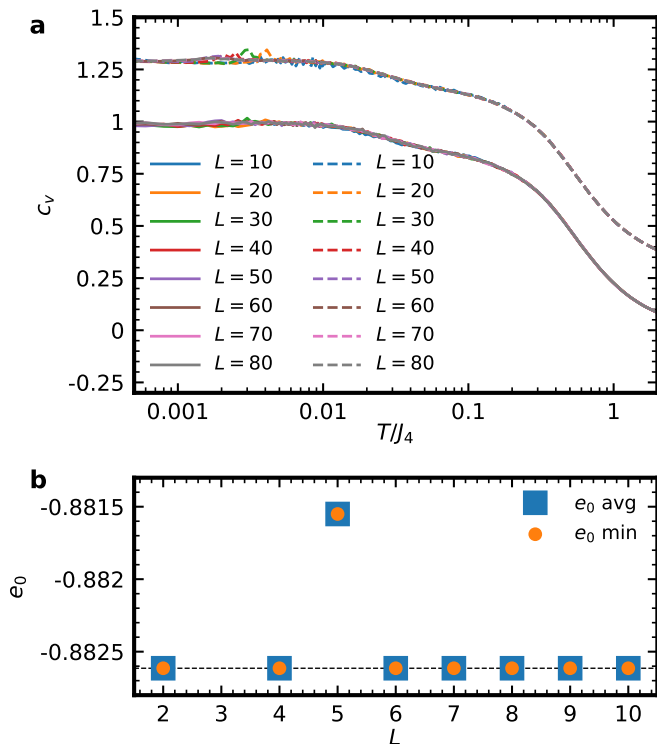
Supplementary Figure 4. Two classical Monte Carlo configurations for the 2D model at $T = 0$ for $L = 2$. The size and direction of the arrows indicate the (S_x, S_y) component, while the colour of the arrows indicates the S_z component. All spins are rotated so that the apex spin in the bottom left is $(0, 0, 1)$.

represent the variety within the manifold well and give rise to the needle-like features in the spin structure factor (see main text).

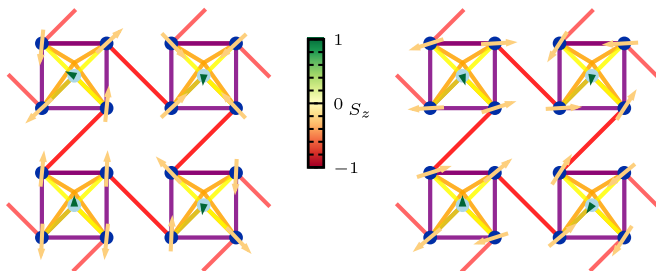
As shown in the main article, the needle-like features in the spin structure factor can be reproduced in an effective model in which $2/7$ of the spins are missing and J_1 and J_6 couplings are neglected while J_3 changed sign (from antiferromagnetic to ferromagnetic). The number of sites for these systems is $N = 5L^2$, because the unit cell now contains only five sites (one pyramid). In Supplementary Figure 5 we show the results for this effective 2D model. In this case, in contrast to the full 2D model, there is no peak at finite temperatures. On the energy side, we see again that even L always gets the same and lowest ground-state energies. On the other hand, odd L reaches higher energies for $L = 3$ and $L = 5$ but is indistinguishable from even L for $L \geq 7$. This implies that the frustration induced by the periodic boundary conditions is quickly released in larger system sizes.

While both models show the same key features in the spin structure factor, their specific heats differ in the presence or absence of a peak. The source of the difference becomes evident when looking at the ground-state configuration, shown in Supplementary Figure 6. The basic pattern is similar to the one in the full 2D model, with all apex spins pointing in the S_z direction and the base spins canted out of the (S_x, S_y) -plane by a small negative value of S_z . The spins diagonal to each other, connected by the orange bond J_4 , have also opposite values of (S_x, S_y) . The only difference in the effective model is that now all zigzag lines are independent, meaning that the spins connected by the purple J_2 bonds can form any angle (and not $\pi/2$ as before); see in Supplementary Figure 6 that they form different angles in different squares. This degeneracy is lifted in the full 2D model by the bonds J_1 , J_6 , and the inclusion of the link sites. This explains the peak observed in the specific heat, corresponding to the temperature at which the angle is locked to $\pi/2$ when the small couplings become relevant.

In conclusion, the effective model has an extra free-



Supplementary Figure 5. Classical Monte Carlo calculations for the 2D effective model for several sizes L . **a** Specific heat is calculated in two different ways (see text), where the dashed data is shifted by 0.3 to appreciate the difference. **b** Ground-state energy average over 10 independent runs (blue squares) and the lowest value among the runs (orange circle).



Supplementary Figure 6. Two classical Monte Carlo configurations for the effective model at $T = 0$ for $L = 2$. The size and direction of the arrows indicate the (S_x, S_y) component, while the colour of the arrows indicates the S_z component. All spins are rotated so that the apex spin in the bottom left is $(0, 0, 1)$.

dom, in which all the spins along a certain zigzag line can be rotated by any angle around the S_z axis and not only by an angle of π as in the full 2D model. This means that the four colouring solutions are still contained within the manifold in the effective model, but the space is larger. However, both systems exhibit the characteristic needle-like features in the spin structure factor because it only depends on the possibility of the system to fluctuate freely along zigzag lines.

Supplementary Note 4. CLASSICAL MONTE CARLO RESULTS ON THE 3D MODEL

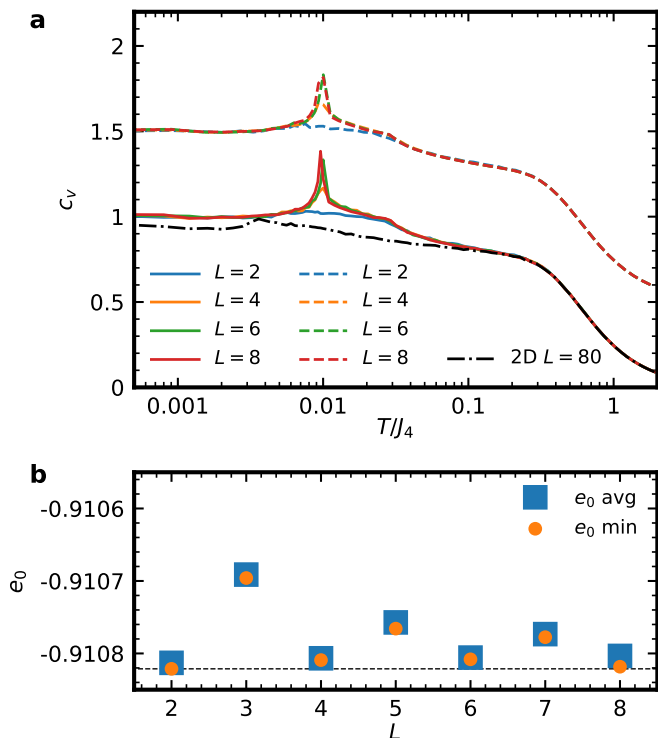
To consider the 3D model that describes nabokoite, we take into account the lattice distortions that affect the structural periodicity. Because on each layer there are pyramids pointing up and down, we take as the layer unit cell an $L = 2$ piece of the 2D model. Furthermore, consecutive layers have exchanged J_1 and J_3 couplings due to the pyramids being slightly rotated clockwise or counterclockwise. Therefore, we need to consider as the unit cell of our 3D system two layers of $L = 2$ in the language of the 2D model, equivalent to $N_u = 7 \times 2^3 = 56$ spins. With this in mind, we make our calculations in systems of $N = 56L^3$ spins with up to $L = 8$ (28672 spins). The rest of the calculations are performed in the same way as for the 2D models.

In Supplementary Figure 7 **a** we show the results for the specific heat calculated in two different ways. Both methods agree in the sense that they exhibit a peak that scales with increasing system size, showing a clear phase transition. Furthermore, we also plot the specific heat for the $L = 40$ 2D model in a dot-dashed black line. It becomes clear that the calculations for the 3D and 2D models start to be different below $T = 0.2 J_4$ when the interlayer coupling J_8 becomes relevant. In Supplementary Figure 7 **b** we show the ground-state energies for different sizes. In this case, all lattices with even L exhibit lower ground-state energies and always the same value as the $L = 2$ system (448 spins). On the other hand, lattices with odd values of L have larger ground-state energies, indicating that there is frustration due to boundary conditions.

In Supplementary Figure 8 we show the spin configuration for the $L = 2$ lattice using the 3D model. This system contains four different layers, which can be seen on the different panels. As shown in the main article, the ground state of the 3D model is different from that of the 2D model. The interlayer coupling J_8 , however small, plays a key role at low temperatures driving a phase transition to a more complicated state. The apex spins are not all ferromagnetically ordered through the system. However, there are some slices in which they (the apex spins) order ferromagnetically (see for example the top row on each layer). Some other slices oppose these spins (see the third row from the top). The complicated structure that minimizes the ground-state energy at $T = 0$ certainly deserves further investigation, which is out of the scope of this work in which we focus on the properties of the 2D regime.

Supplementary Note 5. PMFRG RESULTS

The PMFRG method relies on writing the quantum spin operators in the Majorana fermion representation [S3, S4]. This re-writing has the advantage of not introducing any unphysical enlargement of the Hilbert



Supplementary Figure 7. Classical Monte Carlo calculations for the 3D model for several sizes L . **a** Specific heat is calculated in two different ways (see text), where the dashed data is shifted by 0.5 to appreciate the difference. **b** Ground-state energy average over 10 independent runs (blue squares) and the lowest value among the runs (orange circle).

space, but a trivial degeneracy that can be easily considered. In particular, we use the recently developed temperature-flow PMFRG [S5], in which the temperature T is used as the cutoff parameter which evolves from $T = \infty$ down to lower temperatures. Essentially, the method consists of solving an infinite set of coupled differential equations, known as the flow equations, for the corresponding fermionic vertex functions, from which the spin-spin correlations can be obtained at a given T .

The PMFRG method preserves all symmetries of the original Hamiltonian, and the lattice symmetries can be implemented to reduce considerably the number of flow equations. Within the method, ordering phase transitions at finite temperatures can be detected via finite-size scalings of the correlation length. The latter is obtained directly from the peak in the spin structure factor (or susceptibility). PMFRG has been shown to obtain accurate results for the critical temperature when compared against quasi-exact methods like quantum Monte Carlo [S4, S5].

To solve the 3D model, we use the available atomic positions found in the literature, for which the nearest-neighbour distances are stated in Table 1. We take into account couplings from J_1 to J_8 , which correspond to interatomic distances of 3.102 Å to 5.366 Å. We solve the flow equations for all symmetry-inequivalent spin-

spin correlations contained within a sphere of radius R from the three symmetry-inequivalent Cu sites. In other words, we work on an infinite lattice where we take into account all spin-spin correlations at distances $\leq R$. From these correlations, the spin structure factor can be calculated and subsequently the susceptibility as the values of $S(\mathbf{q}^*; T)$, where \mathbf{q}^* is the wavevector for which the maximum of $S(\mathbf{q})$ can be found.

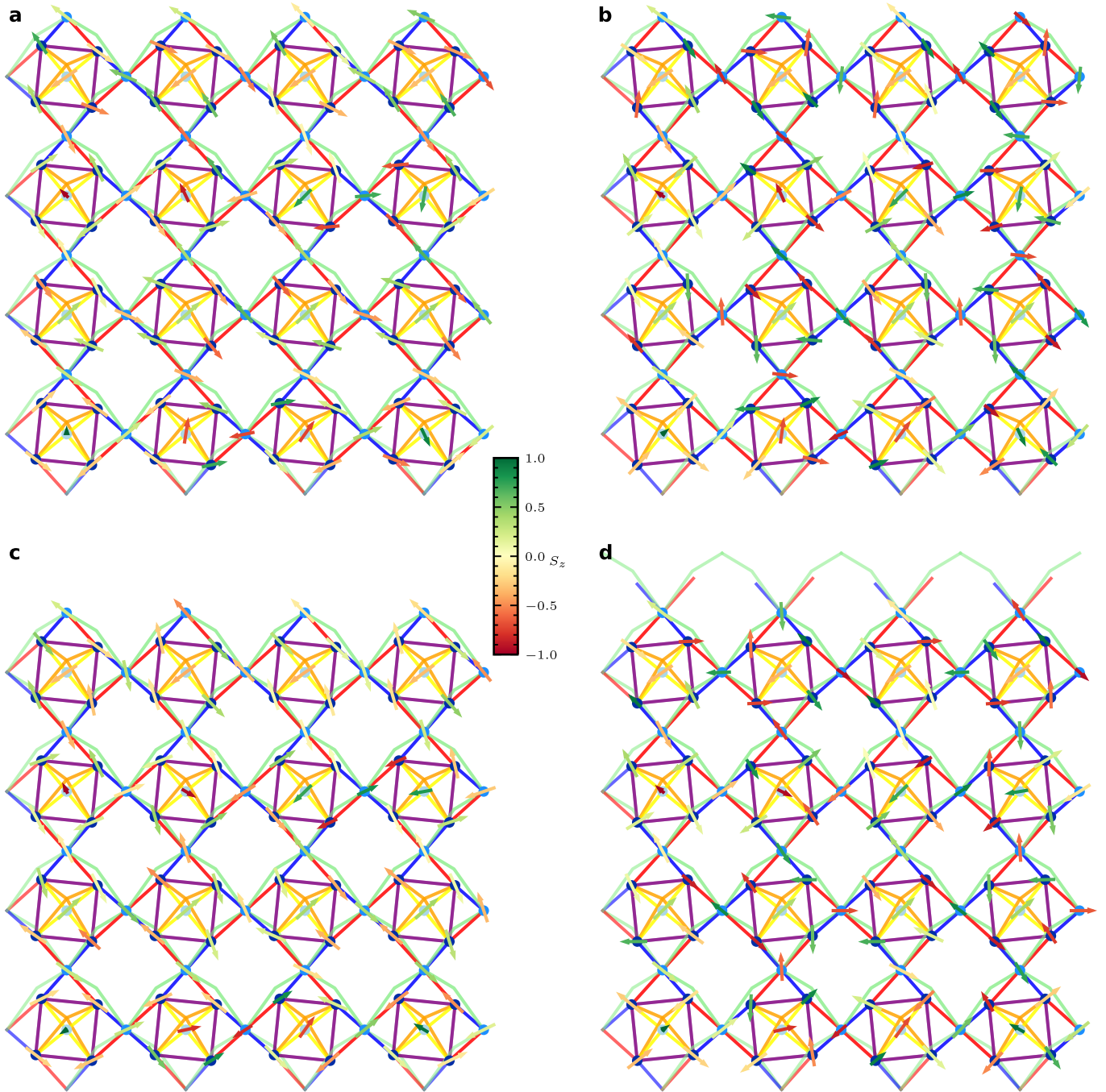
We show in Supplementary Figure 9 the susceptibility in the 3D model as a function of the temperature for several values of R from 6 Å to 20 Å. These imply taking into account between 27 and 823 symmetry-inequivalent correlation pairs. Firstly, no divergency is observed in the temperature range down to $T = 0.01 J_4$, indicating the absence of a phase transition. Furthermore, results are converged for all $R \geq 10$, again indicating that the correlation length does not diverge down to $T = 0.01 J_4$. This does not rule out the existence of a phase transition at lower temperatures, which are not reliably accessible within PMFRG. We also show in the inset the difference between setting the interlayer coupling to zero, $J_8 = 0$, for $R = 20$ Å. The difference that J_8 induces in the susceptibility or spin structure factor is only very small at very small temperatures in the quantum case.

Supplementary Note 6. SINGLE CLASSICAL PYRAMID

In this section, we focus on a single pyramid and ask how the energy can be minimized in such a 5-spin system. We consider the base spins connected with J_2 along the sides and J_4 along the diagonals, while the apex spin is connected by J_5 to the base (the same as in all of our models). Even though every spin in the pyramid interacts with the remaining ones, because of the difference in the couplings $J_2 \neq J_4$, the corresponding 5-spin Hamiltonian cannot be rewritten as a complete square.

First, let us think about the four Cu(1) spins connected in a square with J_2 on the sides and J_4 on the diagonals, disregarding the apex site and the J_5 coupling. This square has two possible solutions depending on the ratio of antiferromagnetic J_2 and J_4 . On one hand, if the diagonal coupling J_4 is smaller than J_2 , the spins minimize the energy by forming a collinear Néel state in the square. On the other, if $J_4 > J_2$ as in the present case, the energy is minimized by a coplanar state in which each diagonal has opposing spins, but the angle between spins in different diagonals is completely free.

Let us assume that the coplanar state on the square is on the xy plane, and let us couple the apex spin pointing in the z direction to the square by increasing J_5 . For $J_5 \rightarrow 0$, the state on the square will remain coplanar. When J_5 increases, the spins on the square will start canting outside the plane, leading to a total net ferrimagnetic moment. The out-of-plane canting angle is shown in Supplementary Figure 10 as a function of J_5 and J_4 . The red star marks the ratio of parameters from the Hamil-

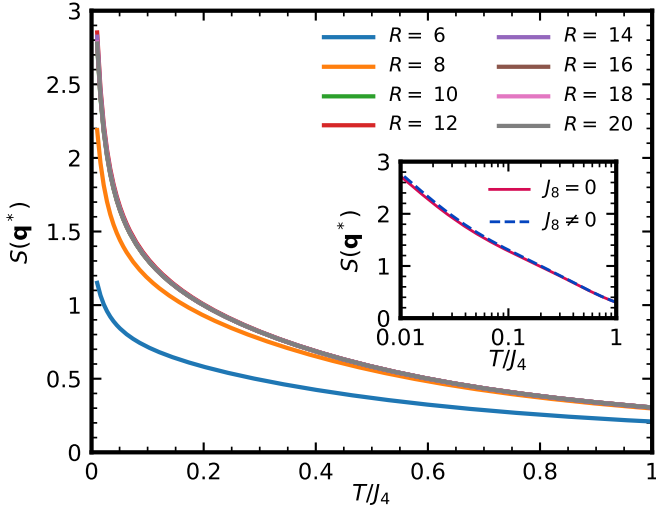


Supplementary Figure 8. Classical Monte Carlo configuration for the 3D model at $T = 0$ for $L = 2$. The layers 1 to 4 are shown in panels **a** to **d**, respectively. The size and direction of the arrows indicate the (S_x, S_y) component, while the colour of the arrows indicates the S_z component. All spins are rotated so that the apex spin in the bottom left of the first layer is $(0, 0, 1)$.

tonian, and the black contour lines indicate three angles close to it. The dashed black line separates the two states described above, also depicted by the squares and spins in Supplementary Figure 10. As $J_5 \rightarrow \infty$, both states become the same: the centre spin pointing up and all the rest pointing down.

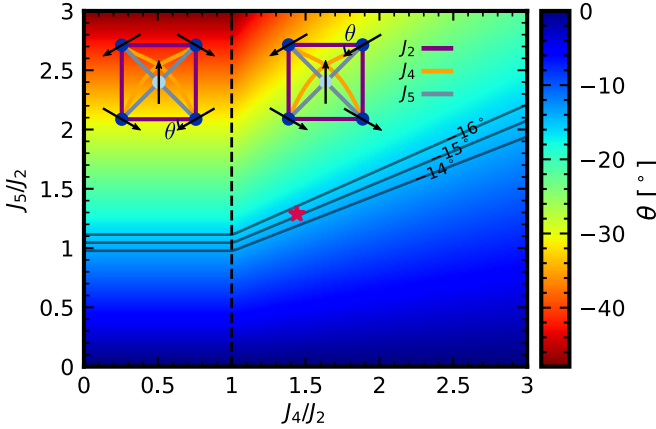
Supplementary Note 7. FROM THE 2D TO THE 3D SPIN STRUCTURE FACTOR

Here we illustrate how the spin structure factor observed in the simple 2D model without lattice distortions looks like when considering different layers with opposite chirality in the 3D model as well as lattice distortions. In Supplementary Figure 11 we show cMC results for



Supplementary Figure 9. PMFRG temperature flows for the 3D model for different values of R (in Å). For each case, \mathbf{q}^* corresponds to the point in reciprocal space for which the highest value of the spin structure factor is observed. The inset shows the difference between the 3D model and taking $J_8 = 0$ for $R = 20$.

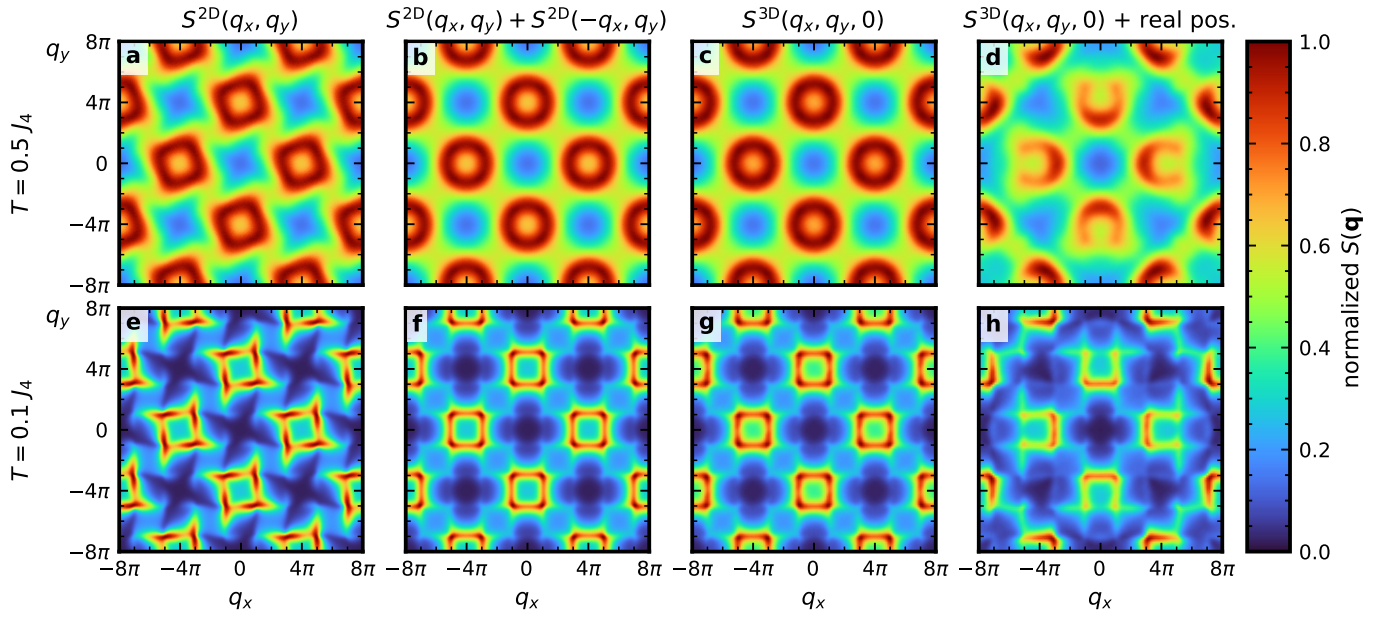
Another interpretation is that this is the structure factor that would be observed if the layers are completely decoupled or if $J_8 = 0$. In the third column (panels c and g) we show the actual calculations on the 3D model, which make evident that J_8 is not playing any role at these temperatures and the spin structure factors are the same as in the 2D model. In other words, there is a two-dimensionalization effect led by the temperature. Finally, in the last column, we show the spin structure factor of the 3D model taking into account the atomic positions of the Cu atoms. This shifts the weight in the spin structure factor and makes it non-periodic (as can be seen in the main article). It can be seen that the change in the positions within the unit cell redistributes the weight on the rings, transforming them into the horseshoe features shown in the main article. However, we stress that the atomic positions only change the appearance of the spin structure factor and not the spin-spin correlations themselves, which only depend on the Hamiltonian (that is unchanged).



Supplementary Figure 10. Canting angle as a function of J_4 and J_5 for a single classical pyramid. The lattices at each side of the dashed line depict the states. The red star indicates the values for the $\text{KCu}_7\text{TeO}_4(\text{SO}_4)_5\text{Cl}$ compound.

the spin structure factor at two different temperatures, $T = 0.5 J_4$ and $T = 0.1 J_4$, in two different rows. The first column contains the same results shown in the main article for the 2D model, where the lattice is simplified with respect to the structure of the $\text{KCu}_7\text{TeO}_4(\text{SO}_4)_5\text{Cl}$ compound. This is done to work with a periodic spin structure factor and with square sublattices in the structure, which in time allows us to interpret more easily the results.

In the second column (panels b and f), we show the result of symmetrizing the spin structure factor to take into account different layers with opposing chirality of couplings (exchanging J_1 and J_3 triangular couplings).



Supplementary Figure 11. Spin structure factor obtained with cMC for two different temperatures, $T = 0.5 J_4$ (a-d) and $T = 0.1 J_4$ (e-h). The first column (a,e) corresponds to the 2D model, and the second (b-f) also corresponds to the 2D model but is symmetrized to consider the two chiralities of successive layers. The third column (c,g) corresponds to the 3D model without taking into account the real positions of the spins in $\text{KCu}_7\text{TeO}_4(\text{SO}_4)_5\text{Cl}$. The last column (d,h) considers the atomic positions.

-
- [S1] M. Markina, P. Berdonosov, T. Vasilchikova, K. Zakharov, A. Murtazoev, V. Dolgikh, A. Moskin, V. Glazkov, A. Smirnov, and A. Vasiliev, Static and resonant properties of decorated square kagomé lattice $\text{KCu}_7(\text{TeO}_4)(\text{SO}_4)_5\text{Cl}$, *Mater. Chem. Phys.* **319**, 129348 (2024).
- [S2] R. Pohle and L. D. C. Jaubert, Curie-law crossover in spin liquids, *Phys. Rev. B* **108**, 024411 (2023).
- [S3] N. Niggemann, B. Sbierski, and J. Reuther, Frustrated quantum spins at finite temperature: Pseudo-Majorana functional renormalization group approach, *Phys. Rev. B* **103**, 104431 (2021).
- [S4] N. Niggemann, J. Reuther, and B. Sbierski, Quantitative functional renormalization for three-dimensional quantum Heisenberg models, *SciPost Phys.* **12**, 156 (2022).
- [S5] B. Schneider, J. Reuther, M. G. Gonzalez, B. Sbierski, and N. Niggemann, Temperature flow in pseudo-Majorana functional renormalization for quantum spins, *Phys. Rev. B* **109**, 195109 (2024).